

See discussions, stats, and author profiles for this publication at: <https://www.researchgate.net/publication/51683863>

Enhanced Luminescent Iridium(III) Complexes Bearing Aryltriazole Cyclometallated Ligands

ARTICLE in INORGANIC CHEMISTRY · SEPTEMBER 2011

Impact Factor: 4.76 · DOI: 10.1021/ic2014013 · Source: PubMed

CITATIONS

70

READS

57

3 AUTHORS:



Sébastien Ladouceur

Université de Sherbrooke

16 PUBLICATIONS 339 CITATIONS

SEE PROFILE



Daniel Fortin

Université de Sherbrooke

82 PUBLICATIONS 1,218 CITATIONS

SEE PROFILE



Eli Zysman-Colman

University of St Andrews

68 PUBLICATIONS 718 CITATIONS

SEE PROFILE

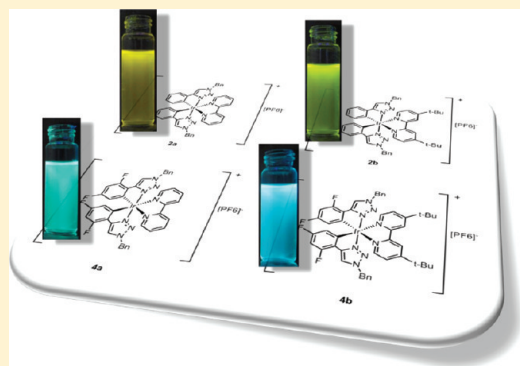
Enhanced Luminescent Iridium(III) Complexes Bearing Aryltriazole Cyclometallated Ligands

Sébastien Ladouceur, Daniel Fortin, and Eli Zysman-Colman*

Département de chimie, Faculté des Sciences, Université de Sherbrooke, 2500 Blvd de l'Université, Sherbrooke J1K 2R1, Canada

Supporting Information

ABSTRACT: Herein we report the synthesis of 4-aryl-1-benzyl-1*H*-1,2,3-triazoles (atl), made via “Click chemistry” and their incorporation as cyclometallating ligands into new heteroleptic iridium(III) complexes containing diimine ($N^{\wedge}N$) ancillary ligands 2,2'-bipyridine (bpy) and 4,4'-di-*tert*-butyl-2,2'-bipyridine (dtbBpy). Depending on decoration, these complexes emit from the yellow to sky blue in acetonitrile (ACN) solution at room temperature (RT). Their emission energies are slightly blue-shifted and their photoluminescent quantum efficiencies are markedly higher (between 25 and 80%) than analogous $(C^{\wedge}N)_2Ir(N^{\wedge}N)^+$ type complexes, where $C^{\wedge}N$ is a decorated 2-phenylpyridinato ligand. This increased brilliance is in part due to the presence of the benzyl groups, which act to sterically shield the iridium metal center. X-ray crystallographic analyses of two of the atl complexes corroborate this assertion. Their electrochemistry is reversible, thus making these complexes amenable for inclusion in light-emitting electrochemical cells (LEECs). A parallel computational investigation supports the experimental findings and demonstrates that for all complexes included in this study, the highest occupied molecular orbital (HOMO) is located on both the aryl fragment of the atl ligands and the iridium metal while the lowest unoccupied molecular orbital (LUMO) is located essentially exclusively on the ancillary ligand.

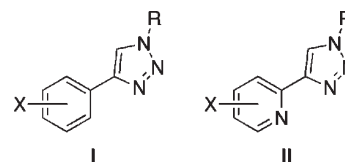


INTRODUCTION

Since the seminal work of Watts and co-workers¹ in the late 1980s to early 1990s, interest in the photophysical and electrochemical properties of cationic heteroleptic iridium complexes of the form $[(ppy)_2Ir(bpy)]^+$, where ppyH is 2-phenylpyridine and bpy is 2,2'-bipyridine, has increased tremendously.² Owing to the large ligand field splitting and the strong spin orbit coupling present in these iridium(III) complexes, color tuning is rendered facile for these phosphors. This class of compounds has thus been readily incorporated into the construction of a myriad of devices.³

The principal strategy for emission energy tuning of iridium(III)-based luminophores has relied on the decoration of either the cyclometallating ligands and/or the ancillary ligand with either electron-donating or electron-withdrawing groups. Far less explored is modification of the heterocycle itself. Those heterocycles investigated to date as ligands about iridium include: 3-pyridyl-1,2-pyrazoles,⁴ 1-aryl-1,2-pyrazoles,^{4c,d,5} pyridyl-imidazoles,^{5a,6} phenyl-imidazoles,⁷ pyridyl-1,2,4-triazoles,^{4a,c,8} 5-aryl-1,2,4-triazoles,⁹ and pyridyl-1,2,3,4-tetrazoles.^{4a,10} There is a particular paucity of examples for the use of aryl-1,2,3-triazoles (I) and/or pyridyl-1,2,3-triazoles (II) in luminophoric complexes, iridium or otherwise.¹¹ In fact, concurrent with our own efforts, only very recently have I^{12} or II^{13} (R = alkyl, benzyl, phenyl or steroidyl) been investigated as ligands about iridium(III), notably by the de Cola and Schubert groups. In light of the increasing interest in the use of triazole ligands on iridium, a detailed structure–property investigation would seem to be warranted. The incorporation of

triazole-based ligands into luminophore design would seem particularly astute given their facile and generalized synthesis via “Click” chemistry, their similar binding motifs to well-studied pyridine substrates, and the predicted blue-shift in emission energy compared to pyridine conferred by the more electron-rich triazole ($pK_a(H_2O)$ 1,2,3 triazole = 9.3; $pK_a(H_2O)$ pyridinium = 5.2).

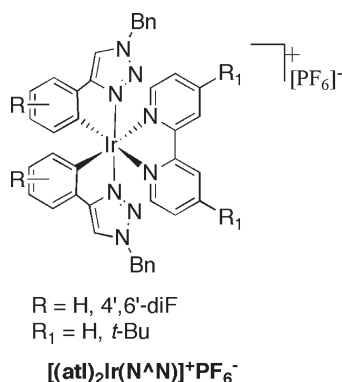


In this paper, we report the synthesis, photophysical and electrochemical properties of a series of $[(atl)_2Ir(N^{\wedge}N)]^+(PF_6)^-$ complexes (Chart 1), where atl is an aryl-1*H*-1,2,3-triazole cyclometallating ligand and $N^{\wedge}N$ is a diimine ligand. The properties of these complexes are compared to archetypal $[(C^{\wedge}N)_2Ir(N^{\wedge}N)]^+(PF_6)^-$ complexes, wherein $C^{\wedge}N$ is either a 2-phenylpyridinato (ppy, complexes 1a and 1b) or a 2-(2,4-difluorophenyl)-5-methylpyridinato (dFMeppy, complexes 3a and 3b) ligand. We demonstrate that the electrochemical gap can be easily tuned resulting in complexes that emit from the yellow to sky blue. To our knowledge, the complexes presented herein are among the brightest known at each of their respective wavelengths in acetonitrile solution. We attribute the increased quantum yields to steric shielding of

Received: July 6, 2011

Published: September 30, 2011

Chart 1. Structure of Heteroleptic Iridium Complexes Bearing Chelating Aryltriazole (atl) Ligands



the benzyl groups (I, $R = \text{Bn}$) about the iridium center. Crystal structure analysis of two of the complexes corroborates this hypothesis. Cyclic voltammetry studies reveal reversible oxidation and reduction waves, making these complexes appropriate for incorporation into light-emitting electrochemical cells (LEECs). A combined density functional theory (DFT) and time-dependent DFT (TD-DFT) study elucidates the origin of the transitions involved in both absorption and emission for these complexes. These transitions were found to be an admixture of metal-to-ligand charge transfer/ligand-to-ligand charge transfer (MLCT/-LLCT) transitions, similar to transitions found in analogous $[(\text{ppy})_2\text{Ir}(\text{bpy})]^+$ complexes.

EXPERIMENTAL SECTION

General Procedures. Commercial chemicals were used as supplied. All experiments were carried out with freshly distilled anhydrous solvents obtained from a Pure Solv solvent purification system from Innovative Technologies except where specifically mentioned. Triethylamine (Et_3N) and di-*iso*-propylamine ($i\text{Pr}_2\text{NH}$) were distilled over CaH_2 under a nitrogen atmosphere. Solvents employed for the Click reaction were used without further purification: these consisted of commercial lab grade methanol and deionized water, which was accessible in house. Aryltriazoles were prepared following a one-pot protocol¹⁴ while 2-(2,4-difluorophenyl)-5-methylpyridine (dFMepyH) was obtained via a Kröhnke condensation.¹⁵

All reactions were performed using standard Schlenk techniques under an inert (N_2) atmosphere, save for the Click reactions. Flash column chromatography was performed using silica gel (Silica-P from Silicycle, 60 Å, 40–63 μm). Analytical thin layer chromatography (TLC) was performed with silica plates with aluminum backings (250 μm with indicator F-254). Compounds were visualized under UV light. ^1H and ^{13}C NMR spectra were recorded on either a Bruker Avance spectrometer at 400 and 100 MHz, respectively, or a Bruker Avance spectrometer at 300 MHz and 75 MHz, respectively. The following abbreviations have been used for multiplicity assignments: “s” for singlet, “d” for doublet, “t” for triplet, “m” for multiplet, and “br” for broad. Deuterated chloroform (CDCl_3) was used as the solvent of record except where noted below. Spectra were referenced to the solvent peak. Melting points (Mp) were recorded using open-end-capillaries on a Melttemp melting point apparatus and are uncorrected. GC-MS samples were separated on a Shimadzu QP 2010 Plus equipped with a HP5-MS 30 m \times 0.25 mm ID \times 0.25 μm film thickness column. Accurate mass measurements were performed on a LC-MSD-TOF instrument from Agilent Technologies in positive electrospray mode. Protonated molecular ions ($\text{M}+\text{H}^+$) were used for empirical formula confirmation. Spectra were recorded at the Université de Montréal Mass Spectrometry facility.

Synthesis of $[(\text{C}^{\wedge}\text{N})_2\text{Ir}(\text{N}^{\wedge}\text{N})]^+\text{PF}_6^-$ Complexes. *Method A.* This protocol proceeds via isolation of the μ -dichloro bridged iridium-(III) dimer described by Nonoyama¹⁶ followed by its cleavage with 2 equiv of ancillary $\text{N}^{\wedge}\text{N}$ ligand. The desired complex was obtained as its PF_6^- salt after anion metathesis using NH_4PF_6 . Each complex was purified by flash chromatography on silica gel using a gradient of acetone in DCM (0–10% acetone/DCM). The purified complex was redissolved in a minimum amount of MeOH and precipitated again by adding it to an NH_4PF_6 solution (10 mL; 1 g/10 mL). The solid complex was filtered, washed with water, and dried under vacuum. This protocol was used for the synthesis of **1a**, **1b**, **2a**, **3a**, and **3b**.

Method B. This protocol *does not* require dimer isolation. The corresponding $\text{C}^{\wedge}\text{N}$ ligands (0.58 mmol, 2.2 equiv.) and IrCl_3 (0.27 mmol, 1.0 equiv.) were placed in a mixture of 2-EtOEtOH and H_2O (6/1) for a concentration of about 0.04 M of IrCl_3 . The suspension was degassed repeatedly and placed under N_2 and heated at 110 °C for about 19 h. The corresponding $\text{N}^{\wedge}\text{N}$ ligands (0.30 mmol, 1.1 equiv.) were then added, and the solution was stirred at 110 °C for about 19 h. The colored solution was left to cool to room temperature (RT), diluted with water, and the resulting aqueous phase was washed with portions of Et_2O . The aqueous phase was then heated to 70 °C for about 10 min to remove trace Et_2O and then cooled to RT. To the reaction mixture was added a solution of NH_4PF_6 (10 mL, 6.13 mmol; 1 g/10 mL) with the subsequent formation of a precipitate. Each complex was purified by flash chromatography on silica gel using a gradient of DCM in acetone (0–10%). The purified complex was redissolved in a minimum amount of MeOH and precipitated again by adding it to an NH_4PF_6 solution (10 mL; 1 g/10 mL). The title complex was filtered, washed with water, and dried under vacuum. This protocol was used for the synthesis of **1b**, **2a**, **2b**, **4a**, and **4b**.

(1a) Iridium(III) Bis[2-phenyl-pyridine- N,C^2]-2,2'-bipyridine Hexafluorophosphate. A yellow solid was obtained (304.7 mg, 83% - Method A). R_f : 0.33 (Acetone/DCM (1/9)). ^1H NMR (400 MHz, CDCl_3) δ (ppm): 8.66 (d, $J = 8.2$ Hz, 2H), 8.13 (td, $J = 8.0, 1.6$ Hz, 2H), 7.92 (t, $J = 6.4$ Hz, 4H), 7.76 (td, $J = 8.0, 1.3$ Hz, 2H), 7.68 (d, $J = 7.8$ Hz, 2H), 7.49 (d, $J = 5.4$ Hz, 2H), 7.40 (t, $J = 6.1$ Hz, 2H), 7.03 (t, $J = 6.7$ Hz, 4H), 6.91 (td, $J = 7.4, 1.2$ Hz, 2H), 6.29 (d, $J = 7.5$ Hz, 2H). ^{13}C NMR (75 MHz, CDCl_3) δ (ppm): 155.8, 150.1, 148.6, 139.8, 138.1, 131.7, 130.8, 130.0, 128.0, 127.0, 126.3, 125.4, 124.8, 123.4, 122.7, 119.6. HR-MS ($\text{C}_{32}\text{H}_{24}\text{N}_4\text{Ir}^+$) Calculated: 657.16247; Experimental: 657.16195. The characterization generally matches that found in the literature.¹⁷

(1b) Iridium(III) Bis[2-phenyl-pyridine- N,C^2]-4,4'-di-*tert*-butyl-2,2'-bipyridine Hexafluorophosphate. A yellow solid was obtained (228.8 mg, 76% - Method B). R_f : 0.50 (DCM). Mp: 219 °C. ^1H NMR (400 MHz, CDCl_3) δ (ppm): 8.37 (d, $J = 1.8$ Hz, 2H), 7.88 (d, $J = 7.9$ Hz, 2H), 7.82 (d, $J = 5.8$ Hz, 2H), 7.75 (dt, $J = 7.8, 1.5$ Hz, 2H), 7.66 (dd, $J = 7.8, 1.1$ Hz, 2H), 7.60 (dd, $J = 5.1, 0.7$ Hz, 2H), 7.38 (dd, $J = 5.9, 1.9$ Hz, 2H), 7.08 (ddd, $J = 7.3, 5.9, 1.4$ Hz, 2H), 7.00 (td, $J = 7.6, 1.2$ Hz, 2H), 6.89 (td, $J = 7.4, 1.3$ Hz, 2H), 6.29 (dd, $J = 7.6, 1.0$ Hz, 2H), 1.42 (s, 18H). ^{13}C NMR (101 MHz, CDCl_3) δ (ppm): 167.8, 164.0, 155.9, 151.0, 149.9, 149.3, 143.9, 138.2, 131.9, 130.8, 125.5, 124.8, 123.7, 122.6, 121.8, 119.6, 110.0, 35.9, 30.5. HR-MS ($\text{C}_{40}\text{H}_{40}\text{N}_4\text{Ir}^+$) Calculated: 769.28767; Experimental: 769.28811. The characterization generally matches that found in the literature.¹⁸

(2a). Iridium(III) Bis[1'-phenyl-1,2,3-triazolato- N,C^2]-2,2'-bipyridine Hexafluorophosphate. A yellow solid was obtained (128.3 mg, 50% - Method B). R_f : 0.52 (Acetone/DCM (1/9)). Mp: 182 °C. ^1H NMR (400 MHz, CD_3CN) δ (ppm): 8.46 (dt, $J = 8.1, 1.1$ Hz, 2H), 8.16–8.07 (m, 6H), 7.51 (ddd, $J = 7.5, 1.4, 0.5$ Hz, 2H), 7.47 (ddd, $J = 7.6, 5.5, 1.2$ Hz, 2H), 7.42–7.34 (m, 6H), 7.23–7.18 (m, 4H), 6.99 (td, $J = 7.5, 1.2$ Hz, 2H), 6.85 (td, $J = 7.5, 1.4$ Hz, 2H), 6.25 (ddd, $J = 7.6, 1.1, 0.5$ Hz, 2H), 5.46 (d, $J = 1.9$ Hz, 4H). ^{13}C NMR (75 MHz) δ (ppm): 158.1, 157.5, 152.2, 147.0, 140.0, 136.7, 135.4, 133.4, 130.0,

129.7, 129.2, 128.8, 128.3, 124.6, 123.6, 123.4, 120.8, 56.1. HR-MS ($C_{40}H_{32}N_8Ir^+$) Calculated: 817.23737; Experimental: 817.2382.

(2b). Iridium(III) Bis[1'-(4',6'-difluorophenyl)-1,2,3-triazolato- N,C^2]-4,4'-di-*tert*-butyl-2,2'-bipyridine Hexafluorophosphate. A yellow solid was obtained (228.5 mg, 63% - Method B). R_f : 0.9 (DCM). Mp: 245 °C. 1H NMR (400 MHz, CD_3CN) δ (ppm): 8.45 (d, J = 1.8 Hz, 2H), 8.12 (s, 2H), 7.98 (d, J = 5.8 Hz, 2H), 7.51 (dd, J = 7.5, 1.3 Hz, 2H), 7.48 (dd, J = 5.9, 2.0 Hz, 2H), 7.43–7.33 (m, 6H), 7.29–7.14 (m, 4H), 6.98 (td, J = 7.5, 1.2 Hz, 2H), 6.84 (td, J = 7.5, 1.4 Hz, 2H), 6.24 (dd, J = 7.5, 0.6 Hz, 2H), 5.47 (s, 4H), 1.43 (s, 18H). ^{13}C NMR (75 MHz, CD_3CN) δ (ppm): 164.7, 158.1, 157.4, 151.6, 147.5, 136.6, 135.4, 133.4, 129.9, 129.7, 129.2, 128.8, 125.3, 123.5, 123.4, 121.8, 120.8, 105.7, 56.1, 36.4, 30.4. HR-MS ($C_{48}H_{48}N_8Ir^+$) Calculated: 929.36257; Experimental: 929.36251.

(3a) Iridium(III) Bis[2-(2,4-difluorophenyl)-5-methylpyridine- N,C^2]-2,2'-bipyridine Hexafluorophosphate. A yellow solid was obtained (162.6 mg, 68% - Method A). R_f : 0.43 (Acetone/DCM (1/9)). Mp: 215 °C. 1H NMR (300 MHz, $CDCl_3$) δ (ppm): 8.80 (d, J = 8.2 Hz, 2H), 8.29–8.15 (m, 4H), 7.93 (d, J = 4.1 Hz, 2H), 7.63 (d, J = 6.9 Hz, 2H), 7.50 (t, J = 6.4 Hz, 2H), 7.19 (d, J = 1.0 Hz, 2H), 6.62–6.51 (m, 2H), 5.65 (dd, J = 8.3, 2.4 Hz, 2H), 2.18 (s, 6H). ^{13}C NMR (75 MHz, CD_3CN) δ (ppm): 165.7 (d, J = 12.2 Hz), 163.6 (d, J = 12.5 Hz), 162.1 (dd, J = 33.5, 9.6 Hz), 160.1 (d, J = 12.8 Hz), 156.6 (s), 154.7 (d, J = 5.3 Hz), 151.8 (s), 150.0 (s), 141.1 (s), 140.6 (s), 135.5 (s), 129.5 (s), 125.9 (s), 124.1 (d, J = 19.5 Hz), 114.7 (d, J = 17.6 Hz), 99.5 (t, J = 27.1 Hz), 18.1 (s). HR-MS ($C_{34}H_{24}N_4F_4Ir^+$) Calculated: 757.15608; Experimental: 757.15793.

(3b) Iridium(III) Bis[2-(2,4-difluorophenyl)-5-methylpyridine- N,C^2]-4,4'-di-*tert*-butyl-2,2'-bipyridine Hexafluorophosphate. A yellow solid was obtained (275.7 mg, 57% - Method A). R_f : 0.33 (DCM). Mp: 359 (dec.) °C. 1H NMR (400 MHz, CD_3CN) δ (ppm): 8.52 (d, J = 1.9 Hz, 2H), 8.22 (dd, J = 8.5, 1.7 Hz, 2H), 7.89 (d, J = 5.9 Hz, 2H), 7.76 (dd, J = 8.5, 1.8 Hz, 2H), 7.54 (dd, J = 5.9, 2.0 Hz, 2H), 7.38–7.33 (m, 2H), 6.68 (dd, J = 12.6, 9.4, 2.4 Hz, 2H), 5.75 (dd, J = 8.7, 2.4 Hz, 2H), 2.14 (s, 6H), 1.44 (s, 18H). ^{13}C NMR (101 MHz, CD_3CN) δ (ppm): 165.3 (s), 164.0–162.4 (m), 162.1 (d, J = 7.3 Hz), 160.6 (d, J = 13.0 Hz), 156.5 (s), 155.4 (d, J = 6.4 Hz), 151.2 (s), 149.9 (s), 141.0 (s), 135.4 (s), 129.0 (dd, J = 4.3, 2.9 Hz), 126.3 (s), 124.0 (d, J = 19.5 Hz), 123.3 (s), 114.6 (dd, J = 17.6, 2.9 Hz), 99.3 (t, J = 26.3 Hz), 36.5 (s), 30.4 (s), 18.1 (s). HR-MS ($C_{42}H_{40}N_4F_4Ir^+$) Calculated: 869.28128; Experimental: 869.28462. The characterization generally matches that found in the literature.¹⁹

(4a). Iridium(III) Bis[1'-(4',6'-difluorophenyl)-1,2,3-triazolato- N,C^2]-2,2'-bipyridine Hexafluorophosphate. A yellow solid was obtained (185.6 mg, 64% - Method B). R_f : 0.45 (Acetone/DCM (1/9)). Mp: 183 °C. 1H NMR (300 MHz, CD_3CN) δ (ppm): 8.46 (d, J = 8.1 Hz, 2H), 8.21–8.03 (m, 6H), 7.50 (t, J = 6.4 Hz, 2H), 7.40–7.31 (m, 6H), 7.24–7.05 (m, 4H), 6.67 (td, J = 10.1, 1.6 Hz, 2H), 5.77 (dd, J = 8.9, 1.7 Hz, 2H), 5.48 (s, 4H). ^{13}C NMR (75 MHz, CD_3CN) δ (ppm): 165.6 (d, J = 11.7 Hz), 162.2 (d, J = 10.6 Hz), 160.0 (d, J = 12.4 Hz), 157.3 (s), 156.6 (d, J = 12.8 Hz), 153.2 (s), 152.6 (s), 150.9 (d, J = 4.9 Hz), 140.6 (s), 135.2 (s), 129.9 (d, J = 13.5 Hz), 128.7 (d, J = 7.3 Hz), 124.8 (s), 122.7 (s), 115.8 (d, J = 18.5 Hz), 105.7 (s), 98.9 (t, J = 25.5 Hz), 56.3 (s). HR-MS ($C_{40}H_{28}N_8F_4Ir^+$) Calculated: 889.19968; Experimental: 889.19969.

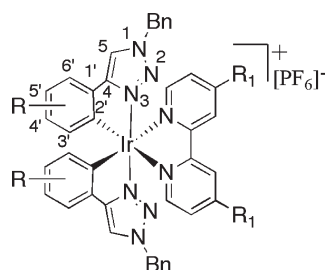
(4b). Iridium(III) Bis[1'-(4',6'-difluorophenyl)-1,2,3-triazolato- N,C^2]-4,4'-di-*tert*-butyl-2,2'-bipyridine Hexafluorophosphate. A yellow solid was obtained (513.7 mg, 44% - Method B). R_f : 0.20 (Et₃N/DCM/Hexanes (4/48/48)). Mp: 236 °C. 1H NMR (300 MHz, CD_3CN) δ (ppm): 8.44 (d, J = 1.9 Hz, 2H), 8.17 (d, J = 1.4 Hz, 2H), 7.98 (d, J = 5.8 Hz, 2H), 7.48 (dd, J = 5.9, 2.0 Hz, 2H), 7.38–7.30 (m, 6H), 7.24–7.15 (m, 4H), 6.66 (td, J = 9.9, 2.2 Hz, 2H), 5.77 (dd, J = 8.9, 2.2 Hz, 2H), 5.49 (s, 4H), 1.43 (s, 18H). ^{13}C NMR (75 MHz, CD_3CN) δ (ppm): 165.56 (d, J = 11.1 Hz), 165.3 (s), 162.2 (d, J = 10.8 Hz),

160.0 (d, J = 13.1 Hz), 157.2 (s), 156.6 (d, J = 12.7 Hz), 153.2 (s), 152.0 (s), 151.4 (d, J = 3.9 Hz), 135.2 (s), 129.8 (d, J = 10.7 Hz), 125.5 (s), 122.7 (s), 122.0 (s), 115.7 (d, J = 18.3 Hz), 98.8 (t, J = 25.6 Hz), 56.3 (s), 36.4 (s), 30.4 (s). HR-MS ($C_{48}H_{44}N_8F_4Ir^+$) Calculated: 1001.32488; Experimental: 1001.32511.

X-ray Crystallography. The crystals for **2a**, **4a** were grown by slow evaporation of a dichloromethane/acetone solvent mixture while crystals for **3b** were grown from a chloroform solution. One single crystal of 0.30 mm \times 0.20 mm \times 0.05 mm for **2a**, one single crystal of 0.20 mm \times 0.30 mm \times 0.50 mm for **4a**, and one single crystal of 0.20 mm \times 0.30 mm \times 0.70 mm for **3b** were each individually mounted using a glass fiber on the goniometer. Data were collected on an Enraf-Nonius CAD-4 automatic diffractometer at the Université de Sherbrooke using ω scans at 198(2) K. The DIFRAC²⁰ program was used for centering, indexing, and data collection. One standard reflection was measured every 100 reflections, no intensity decay was observed during data collection. The data were corrected for absorption by empirical methods based on ψ scans and reduced with the NRCVAX²¹ programs. They were solved using SHELXS-97²² and refined by full-matrix least-squares on F^2 with SHELXL-97.²² The non-hydrogen atoms were refined anisotropically. The hydrogen atoms were placed at idealized calculated geometric position and refined isotropically using a riding model. A summary of the refinement parameters and the resulting factors for **2a**, **4a** and **3b** is given in Supporting Information, Table S1 and ORTEP drawings for each of **2a**, **3b** and **4a** at 30% probability are given in Figures S1, S2 and S3, respectively.

Density Functional Theory (DFT) Calculations. Calculations were performed with Gaussian 09²³ at the Université de Sherbrooke with Mammouth super computer supported by le Réseau Québécois de Calculs de Haute Performances. The DFT²⁴ and TD-DFT²⁵ were calculated with the B3LYP²⁶ method; excited-state triplet geometries were calculated using the unrestricted B3LYP method (UB3LYP). The 3-21G²⁷ basis set was used for C, H and N, and the VDZ (valence double ζ) with SBKJC effective core potential^{27a,28} basis set was used for Iridium. The predicted phosphorescence wavelengths were obtained by energy differences between the Triplet and Singlet optimized states.²⁹ The energy, oscillator strength and related MO contributions for the 100 lowest singlet–singlet excitations were obtained from the TD-DFT/Singlets output file. The calculated absorption spectra was visualized with GaussSum 2.1 (fwhm: 1000 cm^{−1}).³⁰

Photophysical Characterization. All samples were prepared in either HPLC grade acetonitrile (ACN) or a mixture of spectroscopic grade methanol (MeOH) and ethanol (EtOH), with concentrations on the order of 25 μ M. Absorption spectra were recorded at RT and at 77 K in a 1.0 cm capped quartz cuvette and an NMR tube, respectively, using a Shimadzu UV-1800 double beam spectrophotometer. Molar absorptivity determination was verified by linear least-squares fit of values obtained from at least three independent solutions at varying concentrations with absorbances ranging from 0.01–2.6 M. Steady-state emission spectra were obtained by exciting at the longest wavelength absorption maxima using a Horiba Jobin Yvon Fluorolog-3 spectrofluorometer equipped with double monochromators and a photomultiplier tube detector (Hamamatsu model R955). Emission quantum yields were determined using the optically dilute method.³¹ A stock solution for each complex with an absorbance of about 0.5 was prepared and then four dilutions were obtained with dilution factors of 40, 20, 13.3, and 10 resulting in optical dilution absorbances of about 0.013, 0.025, 0.038, and 0.05, respectively. The Beer–Lambert law was assumed to remain linear at the concentrations of the solutions. The emission spectra were then measured after the solutions were rigorously degassed with solvent-saturated nitrogen gas (N₂) for 20 min prior to spectrum acquisition using septa-sealed quartz cells from Starna. For each sample, linearity between absorption and emission intensity was verified through linear regression analysis and additional measurements

Table 1. Structure and Isolated Yields of $[(\text{atI})_2\text{Ir}(\text{N}^{\wedge}\text{N})]^+(\text{PF}_6)^-$ Complexes

compound	R	R1	isolated yield	
			method A ^a	method B ^a
2a	H	H	40%	50%
2b	H	<i>t</i> -butyl		63%
4a	4',6'-difluoro	H		64%
4b	4',6'-difluoro	<i>t</i> -butyl		44%

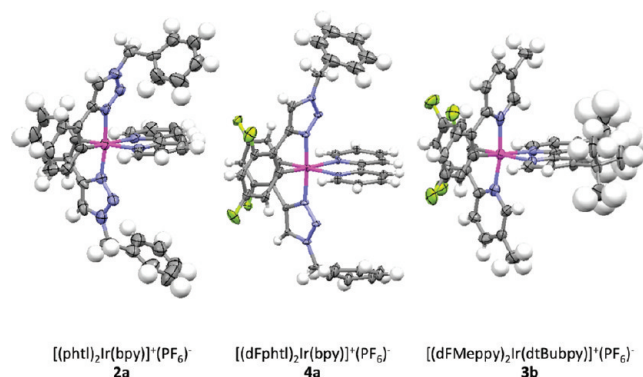
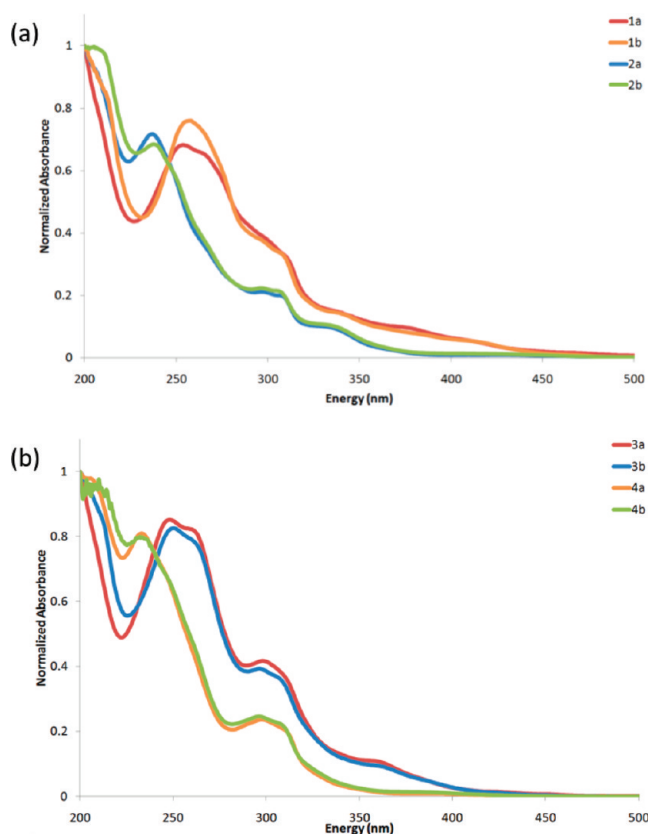
^a See text.**Table 2.** Selected Bond Distances (Å) and Angles (deg) for 1a, 3b, 2a, and 4a

complex	1a ^a	3b	2a	4a
Ir–C _{C^N}	2.004	2.037	1.980	1.999
	2.024	2.057	2.039	2.055
Ir–N _{C^N}	2.042	1.988	1.988	1.988
	2.047	2.040	2.000	1.988
Ir–N _{N^N}	2.129	2.158	2.106	2.123
	2.136	2.194	2.150	2.134
N _{C^N} –Ir–N _{C^N}	172.1	171.6	174.4	173.2
C _{C^N} –Ir–N _{C^N}	80.1	78.7	96.2	94.5
	80.7	79.4	98.2	97.7
N _{N^N} –Ir–N _{N^N}	76.2	74.7	76.3	77.0

^a Data taken from ref 17.

were acquired until the Pearson regression factor (R^2) for the linear fit of the data set surpassed 0.9. Individual relative quantum yield values were calculated for each solution and the values reported represent the slope obtained from the linear fit of these results. The equation $\Phi_s = \Phi_r(A_r/A_s) \cdot (I_s/I_r)(n_s/n_r)^2$ was used to calculate the relative quantum yield of the sample, where Φ_r is the absolute quantum yield of the reference, n is the refractive index of the solvent, A is the absorbance at the excitation wavelength, and I is the integrated area under the corrected emission curve. The subscripts s and r refer to the sample and reference, respectively. A solution of $[\text{Ru}(\text{bpy})_3](\text{PF}_6)_2$ in ACN ($\Phi_r = 0.095$)³² was used as the external reference. The experimental uncertainty in the emission quantum yields is conservatively estimated to be 10%, though we have found that statistically we can reproduce PLQYs to 3% relative error.

Time-resolved excited-state lifetime measurements were determined using the time-correlated single photon counting (TCSPC) option of the Jobin Yvon Fluorolog-3 spectrofluorometer. A pulsed NanoLED at 341 nm, (pulse duration < 1 ns; fwhm = 14 nm), mounted directly on the sample chamber at 90° to the emission monochromator, was used to excite the samples, and photons were collected using a FluoroHub single-photon-counting detector from Horiba Jobin Yvon. The luminescence lifetimes were obtained using the commercially available Horiba Jobin Yvon Decay Analysis Software version 6.4.1, included within the

**Figure 1.** ORTEP perspective representations of complexes 2a, 4a, and 3b (ellipsoids at 50% probability). The counterion and solvent molecules have been omitted for clarity.**Figure 2.** (a) Normalized absorption spectra for 1a, 1b, 2a, and 2b in ACN at 298 K; (b) Normalized absorption spectra for 3a, 3b, 4a, and 4b in ACN at 298 K.

fluorometer. Lifetimes were determined through an assessment of the goodness of its mono exponential fit by minimizing the chi-squared function (χ^2) and by visual inspection of the weighted residuals (see Supporting Information, Figure S4).

Electrochemical Characterization. Cyclic voltammetry measurements were performed on an Electrochemical Analyzer potentiostat model 600D from CH Instruments. Solutions for cyclic voltammetry were prepared in ACN and degassed with ACN-saturated nitrogen bubbling for about 15 min prior to scanning. Tetra(*n*-butyl)ammonium-hexafluorophosphate (TBAPF₆; ca. 0.1 M in ACN) was used as the supporting electrolyte. It was recrystallized twice from EtOH and dried

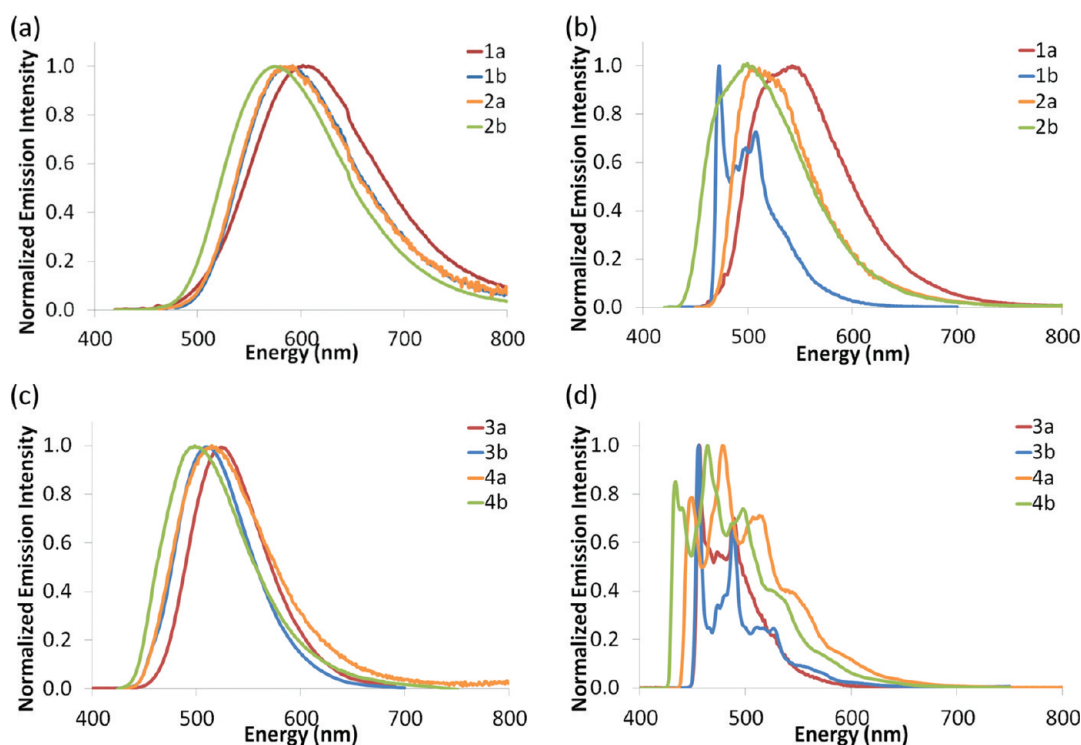


Figure 3. (a) Normalized emission spectra for **1a**, **1b**, **2a**, and **2b** in deaerated ACN at 298 K; (b) Normalized emission spectra for **1a**, **1b**, **2a**, and **2b** in deaerated MeOH:EtOH at 77 K; (c) Normalized emission spectra for **3a**, **3b**, **4a**, and **4b** in deaerated ACN at 298 K; (d) Normalized emission spectra for **3a**, **3b**, **4a**, and **4b** in deaerated MeOH:EtOH at 77 K.

under vacuum prior to use. A nonaqueous Ag/Ag⁺ electrode (silver wire in a solution of 0.1 M AgNO₃ in ACN) was used as the pseudoreference electrode; a glassy-carbon electrode was used for the working electrode and a Pt electrode was used as the counter electrode. The redox potentials are reported relative to a saturated calomel (SCE) electrode with a ferrocenium/ferrocene (Fc⁺/Fc) redox couple as an internal reference (0.40 V vs SCE).³³

RESULTS AND DISCUSSION

Synthesis and Structure. Complex **2a** was synthesized by cleaving the μ -dichloro-bridged iridium(III) dimer [(phtl)₂Ir(μ -Cl)]₂ (phtl = 4-phenyl-1-benzyl-1H-1,2,3-triazole) with 2 equiv of the diimine ligand (N[^]N) in refluxing 2-ethoxyethanol followed by anion metathesis of the chloride salt with NH₄PF₆, analogous to the procedure developed by Nonoyama (Method A).¹⁶ Isolation of the corresponding fluorinated dimer precursors for **4a–4b** proved unsuccessful using this procedure. The heteroleptic complexes were instead obtained via a one-pot two step procedure (Method B) in which IrCl₃ was combined with 2 equiv of dFphtl [dFphtl = 4-(2,4-difluorophenyl)-1-benzyl-1H-1,2,3-triazole] in 2-ethoxyethanol and heated for 19 h at 110 °C, followed by addition of 1 equiv of N[^]N ligand and further heating at 110 °C for 19 h. Upon anion metathesis with NH₄PF₆ the heteroleptic complexes could be isolated in good yield (Table 1). Given its simplicity, this protocol was extended to the synthesis of **2b**. All complexes were characterized by ¹H and ¹³C NMR, which confirmed their C₂ symmetry, and HRMS analyses. Additionally, the crystal structures for **2a** and **4a** and **3b** were obtained to verify the structure.

Single crystals for each of **2a** and **4a** were grown by slow diffusion in a mixed solvent DCM/acetone system and were

characterized by X-ray crystallography. The X-ray structure of each is monoclinic and each crystallized within the P2₁/c space group. Single crystals for **3b** were also obtained by slow evaporation of a chloroform solution. The X-ray structure for **3b** is monoclinic, crystallizing within the P2₁/n space group. A summary of the crystal data and CIF files are available in the Supporting Information. Selected bond lengths and angles for **2a** and **4a** and **3b** are reported in Table 2 and are compared with those for [(ppy)₂Ir(bpy)]PF₆, **1a**. Perspective views for each are shown in Figure 1 and clearly confirm a pseudo-octahedral geometry containing a *cis*-configuration of the aryl groups and a *trans* disposition of the triazole cycles in the atl ligands.

The Ir–C_{atl}, Ir–N_{atl}, and Ir–N_{bpy} bond lengths of complexes **2a** and **4a** are similar to those of **1a** or **3b**. The structural parameters for **4a** in particular mirror those recently reported by De Cola and co-workers for the related [(dFphtl)₂Ir(dMebpy)]PF₆, where dMebpy = 4,4'-dimethyl-2,2'-bipyridine.^{12c} The presence of the fluorine atoms in **3b** and **4a** weakens the Ir–C_{^N} bond somewhat resulting in a slight lengthening when compared (average Ir–C_{^N} = 2.047 and 2.027 Å for **3b** and **4a**, respectively) to **2a** (average Ir–C_{atl} = 2.010 Å). The average C_{atl}–Ir–N_{atl} bite angle for **2a** and **4a** is, respectively, 97.4° and 96.1°, which is substantially larger than those found in **1a**,¹⁷ **3b** or in [(ppz)₂Ir(dtBubpy)]⁺(PF₆)[–] (average C_{ppz}–Ir–N_{ppz} = 80.7°), where ppz = 1-phenylpyrazolyl and dtBubpy = 4,4'-di-*t*-butyl-2,2'-bipyridine.^{5b} The N_{atl}–Ir–N_{atl} bond angle measured between the two triazolyl moieties (174.4° for **2a** and 173.2° for **4a**) resembles that found for the N_{C^N}–Ir–N_{C^N} in **1a** and **3b** (172.1° and 171.6°, respectively). The N_{bpy}–Ir–N_{bpy} bond angle is consistent and was found in all four complexes to be about 76°.

Solution-State Photophysical Properties. Absorption and emission spectra are compiled in Figures 2 and 3, respectively,

Table 3. Photophysical Properties of Complexes under Investigation

complex	ligands		absorbance 298 K (nm) ^a		phosphorescence (λ_{max})		Stokes shifts		quantum yield (Φ)	lifetime (τ)		k_{τ}	k_{nr}
	C ^N	N ^N	[molar absorptivities ($\times 10^4 \text{ M}^{-1} \text{ cm}^{-1}$)]		77 K (nm) ^b	298 K (nm) ^a	77 K (cm^{-1})	298 K (cm^{-1})	(%) ^{ad}	77 K (μs) ^b	298 K (ns) ^a	($\times 10^5 \text{ s}^{-1}$)	($\times 10^5 \text{ s}^{-1}$)
1a	ppy	bpy	265 [4.17]; 310 [1.29]; 375 [0.60]; 420 [0.26]		542	602	5359	7198	9.29	4.77	275	3.4	33
1b	ppy	dtBuppy	255 [7.23]; 300 [3.46]; 340 [1.40]; 415 [0.48]; 465 [0.10]		473	591	364	4585	27.1	4.55	386	7.0	19
2a	phId	bpy	237 [5.54]; 297 [1.58]; 307 [1.61]; 330 [0.78]; 410 [0.07]; 428 [0.07];		503	580	3484	6123	25.1	4.24	209	12	36
2b	phId	dtBuppy	235 [9.63]; 291 [5.95]; 300 [1.77]; 325 [0.86]; 405 [0.08]		498	575	4611	7300	34.6	4.14	800	4.3	8.2
3a	dFMeppy	bpy	250 [4.55]; 260 [4.41]; 300 [2.19]; 355 [0.58]; 420 [0.07]		455	527	1832	4834	61.4	6.56	1068	5.7	3.6
3b	dFMeppy	dtBuppy	250 [5.60]; 295 [2.73]; 360 [0.64]; 420 [0.09]		456	512	1880	4278	77.8	6.48	1187	6.6	1.9
4a	dFphId	bpy	298 [2.30]; 382 [0.08]; 445 [0.04]		475 [448] ^c	514	1419	3017	73.1	4.13	1105	6.6	2.4
4b	dFphId	dtBuppy	215 [7.63]; 235 [5.78]; 300 [1.84]; 375 [0.10]		463 [433] ^c	498	5068	6586	79.7	4.26	1198	6.7	1.7

^a Measured in ACN. ^b Measured in (1/1) MeOH/EtOH glass state. ^c Values in brackets refer to E_{o-o'}. ^d Measured at 298 K using Ru(bpy)₃(PF₆)₂. $\Phi = 9.5\%$ in ACN see ref 32.

^a Measured in ACN. ^b Measured in (1/1) MeOH/EtOH glass state. ^c Values in brackets refer to $E_{0,0}$. ^d Measured at 298 K using Ru(bpy)₃(PF₆)₂ Φ = 9.5% in ACN see ref 32.

and the data are summarized in Table 3. All complexes were found to be readily soluble in ACN, and this is the solvent of record for all RT spectroscopic and electrochemical measurements. Low temperature measurements were conducted in a 1:1 MeOH/EtOH mixture to promote the formation of a glass state. It is important to note that the spectroscopic properties reported in this study for **1a**,^{3,29} **1b**,^{18,29,34} and **3b**^{34,35} generally reproduce those found in the literature. Absorption and emission spectra for each of the individual complexes can be found in the Supporting Information, Figures S5–S12.

The absorption profiles obtained at RT for **2a**, **2b** and **4a**, **4b** resemble, respectively, those of **1a**, **1b** and **3a**, **3b** (Figure 2). Each of the absorption spectra of the 8 complexes in this study exhibits intense bands ($\epsilon > 10^4 \text{ M}^{-1} \text{ cm}^{-1}$) in the ultraviolet region, between 200 and 275 nm. Each of these bands has been assigned to spin-allowed $^1\pi-\pi^*$ ligand-centered (^1LC) transitions centered on both the cyclometallating and the ancillary ligands. The ^1LC band for **2a** and **2b** are blueshifted, respectively, by about 30 and 20 nm compared to **1a** and **1b**. Similarly, the ^1LC band for both **4a** and **4b** is hypsochromically shifted by 15 nm compared to **3a** and **3b**. Hypochromic bands found at lower energy have been assigned to both spin-allowed and spin-forbidden admixtures of metal-to-ligand charge-transfer ($^1\text{MLCT}$ and $^3\text{MLCT}$) and ligand-to-ligand charge transfer ($^1\text{LLCT}$ and $^3\text{LLCT}$) transitions.^{1a,c,3,36} The lower absorptivities observed for the spin-allowed CT transitions are the result of poor spatial overlap between the highest occupied molecular orbital (HOMO) and the lowest unoccupied molecular orbital (LUMO) (see below for electron density map). These charge transfer-type bands were found to be more intense for the atl C^N ligands than for the arylpyridine ligands (see absorptivities in Table 3).

The RT (298 K) photoluminescence (PL) spectra were obtained in deaerated ACN and are shown in Figures 3a and 3c. Emission energy maxima range from 498 to 602 nm, resulting in perceived emission colors of sky-blue to yellow. The presence of the atl fragment results in a blue-shift of 630 cm^{-1} for **2a** compared to **1a** and 471 cm^{-1} for **2b** compared to **1b**.^{18,29} For the fluorinated analogues, the blue shift is 480 and 549 cm^{-1} , respectively, for **4a** compared to **3a** and **4b** compared to **3b**. The incorporation of the dtBubpy groups results in a relative blueshift 150 and 625 cm^{-1} , respectively, for the nonfluorinated (**2b** compared to **2a**) and fluorinated (**4b** compared to **4a**) complexes. In all cases the PL spectra is broad and featureless, indicative of CT processes. The lack of fine structure in the emission spectra at RT for **4a** and **4b** distinguishes it from other charged heteroleptic iridium complexes emitting at similar wavelengths that exhibit vibronic structure.^{4e,13b} Stokes shifts inferior to 7300 cm^{-1} clearly demonstrate the phosphorescent nature of the emission. The overall effect of the replacement of a ppy-type ligand for an atl-type ligand is a blue shift of between 471 and 630 cm^{-1} .

The PL spectra at 77 K recorded in the MeOH/EtOH glass state are shown in Figures 3b and 3d. The emission maximum ranged from 463 to 542 nm, and each complex exhibits the characteristic rigidochromic blueshift compared to PL spectra obtained at RT. The PL spectra for **2a** and **2b** are broad and featureless. The spectrum for **2b** distinguishes itself from **1b** in that in the latter, fine vibronic structure is observed. All fluorinated analogues (**3a**, **3b**, **4a**, and **4b**) were blueshifted and each spectrum exhibited fine structure, indicative of emission from different vibronic levels in the excited state and a corresponding

Table 4. Electrochemical Properties of 1–4^a

complex	ligands		$E_{1/2,ox}$	ΔE_p	ΔE	$E_{1/2,red}$	ΔE_p
	C [^] N	N [^] N	(V vs SCE)	(mV)	(V vs SCE)	(V vs SCE)	(mV)
1a	ppy	bpy	1.27	56	2.65	−1.38	55
1b	ppy	dtBubpy	1.31	106	2.71	−1.40	87
2a	phtl	bpy	1.28	69	2.75	−1.47	78
2b	phtl	dtBubpy	1.26	84	2.82	−1.56	84
3a	dFMeppy	bpy	1.55	109	2.89	−1.34	84
3b	dFMeppy	dtBubpy	1.51	98	2.94	−1.43	74
4a	dFphtl	bpy	1.61	105	3.01	−1.40	69
4b	dFphtl	dtBubpy	1.60	96	3.09	−1.49	75

^a Measured in ACN (ca. 1.5 mM) with NBu₄PF₆ (ca. 0.1 M) as the supporting electrolyte. Potentials (V) are reported vs an SCE standard electrode and were calibrated using an internal standard Fc/Fc⁺ redox couple (0.40 V in ACN); see ref 33.

increase in LC character for these transitions.^{5b,37} Monoexponentially decaying emission lifetimes for **2a**, **2b**, **4a**, and **4b** are similar to those found for **1a**, **1b**, **3a**, and **3b** and are on the order of 4–6 μ s. Low temperature PL spectra show a moderate-to-large hypsochromic shift resulting from impeded movement of solvent molecules in the glass state (Table 3). This lifetime behavior and the expected blue shift in emission energy suggest that the character of the emission at 77 K remains predominantly an admixture of ³MLCT and ³LLCT. The reorganization of solvent molecules at elevated temperatures about the complex aide in the stabilization of CT states prior to emission.

PL Quantum yields (PLQY, Φ_{pl}) for atl complexes ranged from 25 to 80%. The observed increase in quantum yields is due to a diminution of nonradiative rates with increasing emission energy; an example of the so-called energy-gap law. Striking is the comparison in quantum yield between atl-based complexes and ppy-based complexes. For instance, **2a** is nearly three times as bright as **1a** while **4b** is among the brightest charged heteroleptic iridium complexes emitting in the green-blue region, particularly given that measurements were carried out in ACN.^{4e,5f,6,10,27e,34,38} The observed increase in quantum yields is ascribed to the presence of the benzyl groups on the atl ligand, which sterically shield the iridium about the bipyridine and inhibit nonradiative intermolecular charge recombination.^{3,39} Whereas this strategy has been used effectively by placing large groups on the ancillary ligand,^{3,5a,39,40} incorporation of bulky groups on the cyclometalating ligand that shield the environment of the ancillary ligand has, to our knowledge, rarely been previously reported.^{12a,c} The PL quantum yields decrease markedly in aerated ACN solution. For example the quantum yield for **2a** in aerated solution was found to be 11%.

Emission intensity decays monoexponentially at 298 K with lifetimes that are in the submicrosecond-microsecond regime, an indication of the triplet character of the emission process. Whereas **1a** and **2a** exhibit similar lifetimes, the lifetime of **2b** is twice as long as **1b**, ostensibly owing to a synergistic rigidification of the complex because of a favorable interaction between the benzyl and *t*-butyl groups. Fluorinated complexes, which displayed large PLQYs, exhibited longer lifetimes than nonfluorinated analogues. There was little discrimination in lifetimes, however, between **4a** and **4b**.

From the PLQY and lifetimes, it is possible to determine the radiative (k_r) and nonradiative (k_{nr}) rate constants. The increased quantum yield in going from **1a** to **2a** seems to be due to a 3.5 fold increase in the radiative rate constant. By contrast the greater brilliance of **2b** compared to **1b** is ascribed to a decreased by a

factor of about 2.3 in the nonradiative rate constant. Thus, there seems to be an interplay between the *tert*-butyl groups and the atl ligand. The effect of fluorine atom incorporation into the complexes promotes a further decrease in k_{nr} , in keeping with the behavior predicted by the energy gap law. The similar values obtained for k_r for **3a**, **3b**, **4a**, and **4b** would suggest that emission in these four complexes is occurring from a similar excited state.

Electrochemistry. Cyclic voltammetry measurements (CV), obtained in ACN, were performed to probe the nature of the frontier molecular orbitals of the complexes. A summary of the redox potentials is shown in Table 4, measured relative to an internal ferrocene standard (Fc⁺/Fc = +0.40 V vs SCE in ACN). Generally, electrochemical processes were found to be either reversible or quasi-reversible one-electron processes, and CV spectra were found to be reproducible regardless of scan rate (50–200 mV/s). The redox potentials measured for **1a** and **1b**¹⁸ mirror those found in the literature, while that for **3b**³⁴ is offset anodically by about 0.16 V, perhaps owing to a difference in working electrode (glassy carbon vs Pt). Compounds **1a**, **1b**, **2a**, and **2b** exhibited oxidations in the range of 1.26–1.31 V while compounds **3a**, **3b**, **4a**, and **4b** showed oxidations between 1.51 and 1.61 V. The oxidation is assigned to occur on the metal center and on the C[^]N ligands. The more difficult oxidation of the metal and C[^]N ligands for **3a**, **3b**, **4a**, and **4b** is expected given the electron-withdrawing nature of the fluorine atoms. Generally, the oxidation wave for the atl complex ($E_{1/2,ox}$) was slightly anodically shifted compared to its apy-type congener (apyH = 2-arylpyridine). This anodic shift was more pronounced at about 0.08 V for the comparison between fluorinated complexes (**3a** and **3b** vs **4a** and **4b**) compared to the comparison between nonfluorinated complexes (**1a** and **1b** vs **2a** and **2b**; shift of about 0.02 V). Oddly, whereas the $E_{1/2,ox}$ for the oxidation of **2a** was found to be at 1.28 V, the $E_{1/2,ox}$ for the analogous [(a)₂Ir(bpy)](PF₆) (**5**) was measured to be 1.23 V in DCM vs SHE, which translates to 1.41 V vs SCE (where H-a = 1-decyl-4-phenyl-1H-[1,2,3]triazole).^{12b} This result would suggest that the benzyl group is in fact playing an active role in destabilizing the HOMO in **2a** compared to the decyl group in **5**. For comparison, cationic heteroleptic iridium complexes bearing phenylpyrazole, ppz, cyclometalating ligands, exhibited oxidation potentials at 1.41 V vs SCE.^{5b}

The replacement of bpy for dtBubpy results in a slight cathodic shift of about 0.02 V in the oxidation wave but an expected much larger cathodic shift of about 0.07 V in the first reduction wave, an indication that the LUMO is in large part localized on the

ancillary ligand. The first reduction for each of the complexes is thus assigned to occur on one of the pyridine rings of the $N^{\wedge}N$ ligand. Surprisingly, the replacement of ppy-type ligands for atl-type ligands results in a large cathodic shift of 0.06–0.16 V of the reduction wave. This would indicate that unlike complexes **1a**, **1b**, **3a**, and **3b**, which have been shown to have a LUMO localized essentially only on the ancillary ligand, the LUMO for **2a**, **2b**, **4a**, and **4b** possesses contributions from the metal and/or the cyclometallating ligand. The incorporation of fluorine atoms onto the $C^{\wedge}N$ ligand results in an anodic shift of the reduction

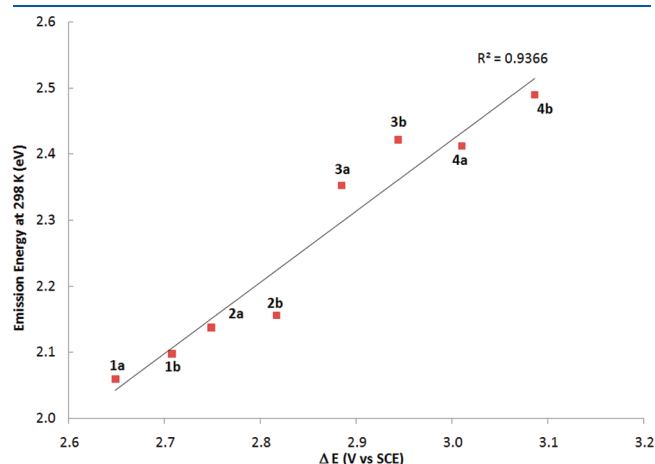


Figure 4. PL emission energy (eV) at RT in ACN compared to $\Delta E_{\text{red-ox}}$ (V) determined by cyclic voltammetry in ACN.

band of about 0.06 V, much smaller than the anodic shift of about 0.28 V for the oxidation wave.

A comparison of the emission energies (λ_{max} in eV) at 298 K with the $\Delta E_{\text{red-ox}}$ reveals the expected linear monotonic relationship (Figure 4). The presence of atl-type ligands, the inclusion of the dtBuppy ligand, and the incorporation of fluorine atoms each have the net effect of increasing the $\Delta E_{\text{red-ox}}$.

Computational Modeling. To gain greater insight into the photophysical and electrochemical properties of the atl-based complexes, a combined DFT/TD-DFT^{24,25} investigation was undertaken at the B3LYP²⁶ level of theory using the SBKJC-DVZ basis set^{27a,28} for Ir and the 3-21G* basis set²⁷ for all other heavy atoms using Gaussian 09 suite.²³ We have previously shown this computational approach to be effective in predicting ground- and excited state properties of $(C^{\wedge}N)_2Ir(N^{\wedge}N)^+$ -type complexes.³ Figures 5 and 6 show the relative orbital energies and their electronic distribution character for each of the 8 complexes. From an evaluation of these MOs, we can assign the origin of the dominant absorption and emission transitions that are observed in the photophysical study. For all the complexes, the HOMO corresponds to a mixture of phenyl $\pi_{C^{\wedge}N}$ and Ir d orbitals. The metal contributions for the HOMO, HOMO-1, and HOMO-2 are of d_{xy} , d_{yz} , and d_{xz} symmetry, in accordance with ligand field theory for the “ t_{2g} ” orbitals of a metal bearing octahedral symmetry (see Supporting Information). The LUMO is principally composed of a $\pi^*_{N^{\wedge}N}$ orbital with very minor contributions from the Ir d orbital. The small changes in $E_{1/2, \text{red}}$ between **1a**, **1b** and **3a**, **3b** (or **2a**, **2b** and **4a**, **4b**) are a testament to this latter assignment. Thus, there is little electronic overlap between these two MOs. The LUMO+1, which is $\pi^*_{N^{\wedge}N}$ in nature, is

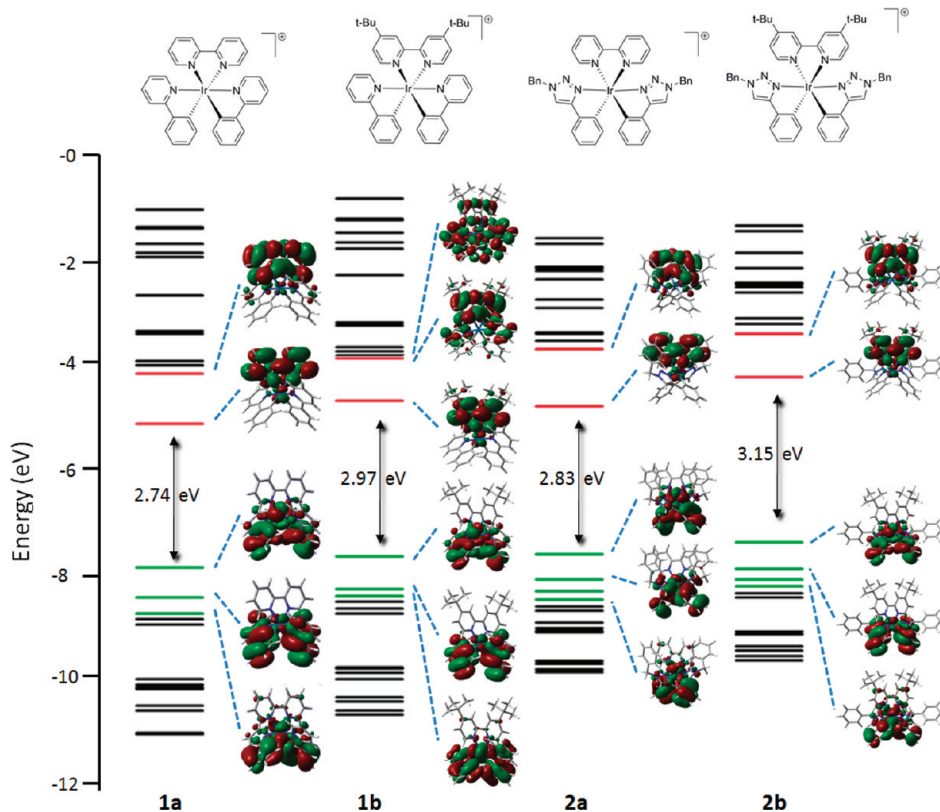


Figure 5. Energy level schemes for the Kohn–Sham orbitals of **1a**, **1b**, **2a**, and **2b**, including the most relevant Kohn–Sham orbitals and the HOMO–LUMO energy gap (see Supporting Information for computational details). Selected MOs have been colored to aid in the analysis. Red indicates that the electron density is primarily localized on the π_{bpy} with minor Ir d π contributions, green on the π_{ppy} or π_{atl} with minor Ir d π contributions.

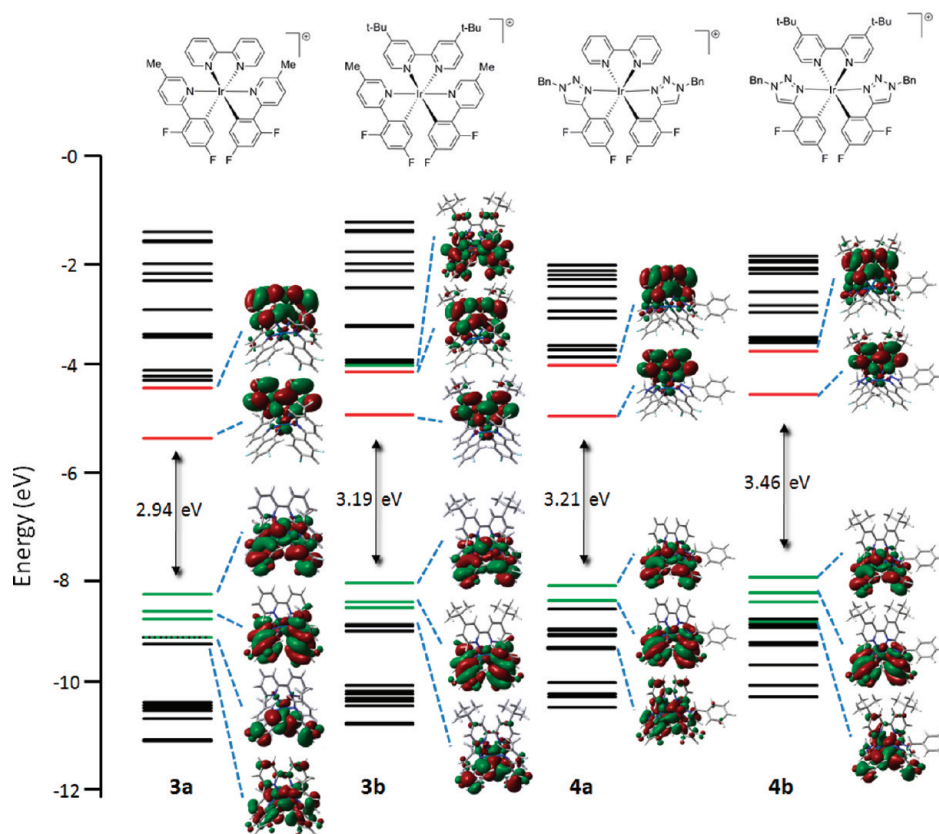


Figure 6. Energy level schemes for the Kohn–Sham orbitals of **3a**, **3b**, **4a**, and **4b**, including the most relevant Kohn–Sham orbitals and the HOMO–LUMO energy gap (see Supporting Information for computational details). Selected MOs have been colored to aid in the analysis. **Red** indicates that the electron density is primarily localized on the π_{bpy} with minor Ir $d\pi$ contributions, **green** on the π_{ppy} or π_{at} with minor Ir $d\pi$ contributions.

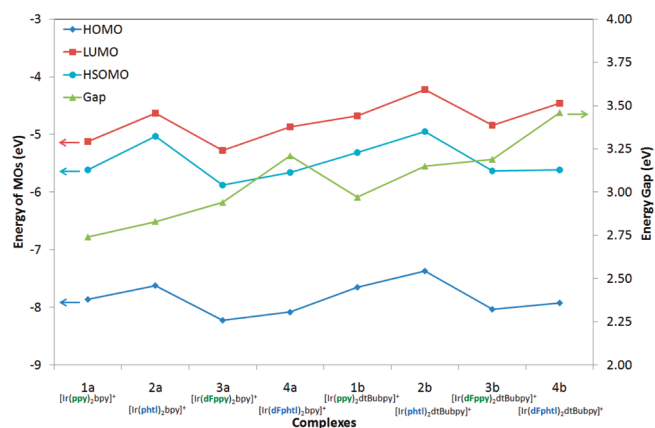


Figure 7. Calculated energies of the $^1\text{HOMO}$ and $^1\text{LUMO}$ and $^3\text{HSOMO}$ for each of the 8 complexes under investigation with the corresponding HOMO–LUMO gap. The lines connecting the data points are placed to increase clarity only.

significantly destabilized by between 0.81 and 0.96 eV, which explains the difficulty in observing the second reduction wave in the CV of these compounds. Probing further the origin of higher energy unoccupied orbitals reveals that they are dominated by $\pi^*_{\text{C}^{\wedge}\text{N}}$ contributions. In fact the greatly destabilized e_g^* orbitals do not even present themselves in the first 7 lowest unoccupied

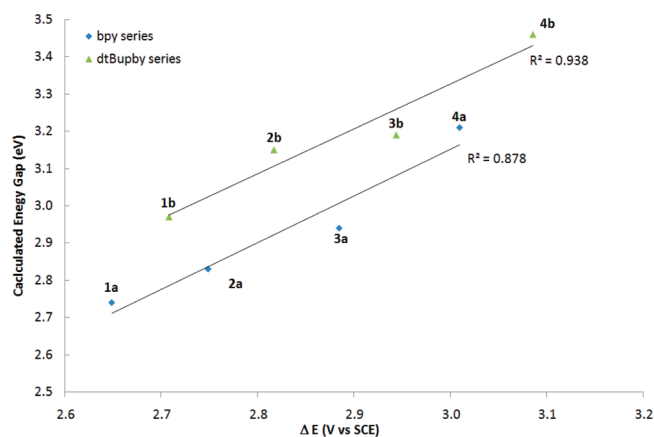


Figure 8. Comparison between the calculated HOMO–LUMO energy gap obtained from the vertical transitions by TD-DFT and the $\Delta E_{\text{red-ox}}$ measured by cyclic voltammetry for each of the 8 complexes, divided into two families based on the identity of the ancillary ($\text{N}^{\wedge}\text{N}$) ligand. The linear fit has also been included.

MOs. In the related complex, **5**, Schubert found that the $5d_{z^2}$ and $5d_{x^2-y^2}$ metal-based orbitals to be at LUMO+11 and LUMO+13, respectively. This expected behavior is due to the strong ligand field splitting character of the cyclometallating ligands and the third row nature of iridium.

Table S. Principal Theoretical Low Energy Electronic Transitions (ΔE), with Corresponding Oscillator Strengths (f), and Assignments for $[(C^{\wedge}N)_2Ir(N^{\wedge}N)]PF_6$

complex	state	ΔE			f	major contributions	assignment	complex	state	ΔE			f	major contributions	assignment
		nm	eV							nm	eV				
1a	S ₁	607.4	2.04	0.0002	0.0002	HOMO \rightarrow LUMO (99%)	LLCT, MLCT	3a	S ₁	555.4	2.23	0.0002	0.0002	HOMO \rightarrow LUMO (98%)	LLCT, MLCT
	S ₃	444.1	2.79	0.0121	0.0121	HOMO-1 \rightarrow LUMO (99%)	LLCT, MLCT		S ₂	453.2	2.74	0.0095	0.0095	HOMO-1 \rightarrow LUMO (99%)	LLCT, MLCT
	S ₄	407.0	3.05	0.0445	0.0445	HOMO-3 \rightarrow LUMO (85%)	LLCT, MLCT		S ₅	389.4	3.18	0.0431	0.0431	HOMO-3 \rightarrow LUMO (61%)	LLCT, MLCT
	S ₁	545.3	2.272	0.0003	0.0003	HOMO \rightarrow LUMO (99%)	LLCT, MLCT		S ₇	379.4	3.27	0.0232	0.0232	HOMO-5 \rightarrow LUMO (33%)	MLCT, LLCT
1b	S ₃	408.6	3.03	0.0292	0.0292	HOMO-1 \rightarrow LUMO (96%)	LLCT, MLCT	3b	S ₇	379.4	3.27	0.0232	0.0232	HOMO-5 \rightarrow LUMO (61%)	MLCT, LLCT
	S ₄	404.9	3.06	0.0305	0.0305	HOMO \rightarrow LUMO+2 (63%)	LC, LLCT, MLCT		S ₈	368.0	3.37	0.0404	0.0404	HOMO-3 \rightarrow LUMO (-37%)	LLCT, MLCT
	S ₇	383.8	3.23	0.054	0.054	HOMO-3 \rightarrow LUMO (79%)	MLCT, LLCT		S ₁	500.8	2.48	0.0003	0.0003	HOMO \rightarrow LUMO (98%)	LLCT, MLCT
	S ₁	538.8	2.30	0.0001	0.0001	HOMO \rightarrow LUMO (99%)	LLCT, MLCT		S ₂	413.1	3.00	0.0198	0.0198	HOMO-1 \rightarrow LUMO (98%)	LLCT, MLCT
2a	S ₂	420.1	2.95	0.0088	0.0088	HOMO-1 \rightarrow LUMO (98%)	LLCT, MLCT		S ₅	373.2	3.32	0.029	0.029	HOMO \rightarrow LUMO+2 (63%)	LC, MLCT
		380.2	3.26	0.0435	0.0435	HOMO-3 \rightarrow LUMO (87%)	LLCT, MLCT							HOMO \rightarrow LUMO+1 (-34%)	LLCT, MLCT
						HOMO-5 \rightarrow LUMO (10%)	LLCT, MLCT		S ₆	368.2	3.37	0.0708	0.0708	HOMO-4 \rightarrow LUMO (63%)	MLCT, LLCT
	S ₁	505.5	2.45	0.0001	0.0001	HOMO \rightarrow LUMO (99%)	LLCT, MLCT							HOMO-5 \rightarrow LUMO (29%)	MLCT, LLCT
2b	S ₂	398.1	3.11	0.0224	0.0224	HOMO-1 \rightarrow LUMO (98%)	LLCT, MLCT	4a	S ₇	366.4	3.38	0.0081	0.0081	HOMO -1 LUMO+1 (64%)	LLCT, MLCT
	S ₅	366.4	3.38	0.0664	0.0664	HOMO-3 \rightarrow LUMO (86%)	LLCT, MLCT							HOMO \rightarrow LUMO+2 (32%)	LC, MLCT
									S ₁	4866	2.55	0.0001	0.0001	HOMO \rightarrow LUMO (97%)	LLCT, MLCT
									S ₂	4183	2.96	0.0137	0.0137	HOMO-1 \rightarrow LUMO (99%)	LLCT, MLCT
									S ₅	357.8	3.46	0.0655	0.0655	HOMO-7 \rightarrow LUMO (57%)	MLCT, LLCT, LC
														HOMO-4 \rightarrow LUMO (37%)	MLCT, LLCT
									S ₁	444.1	2.79	0.0001	0.0001	HOMO \rightarrow LUMO (97%)	LLCT, MLCT
									S ₂	384.4	3.23	0.0247	0.0247	HOMO-1 \rightarrow LUMO (98%)	LLCT, MLCT
									S ₆	340.2	3.64	0.0902	0.0902	HOMO-4 \rightarrow LUMO (61%)	MLCT, LLCT
														HOMO-5 \rightarrow LUMO (25%)	MLCT, LLCT

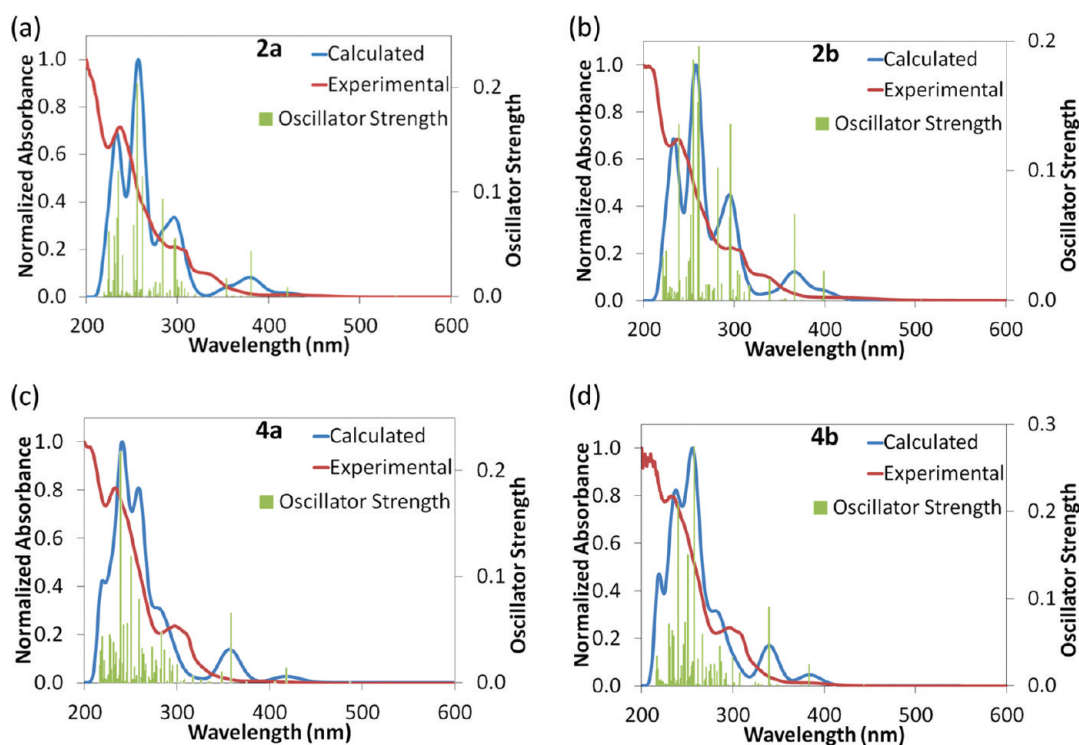


Figure 9. Experimental spectra (red) and simulated (fwhm: 1000 cm^{-1} , blue) absorption spectra for (a) **2a**; (b) **2b**; (c) **4a**; (d) **4b**. The oscillator strengths, calculated by TD-DFT (TD-B3LYP/SBKJC-DVZ on Ir and TD-B3LYP/3-21G* on other heavy atoms), are represented by unbroadened vertical lines of the calculated singlet–singlet transitions (green).

Table 6. Comparison between Calculated Emission Energies (See Text) and Measured Emission Energies at 77 K in I:I MeOH/EtOH

complexes	emission energy						
	calculated						
	eV	nm	77 K	error ^a	298 K		
			eV	nm	(%)	eV	nm
1a	2.21	561	2.29	542	3.4	2.06	602
1b	2.42	513	2.62	473	8.0	2.10	591
2a	2.25	550	2.46	503	8.9	2.14	580
2b	2.52	491	2.49	498	1.3	2.16	575
3a	2.40	516	2.72	455	12.7	2.35	527
3b	2.61	475	2.72	456	4.1	2.42	512
4a	2.67	464	2.77	448	3.5	2.41	514
4b	2.86	434	2.86	433	0.1	2.49	498

^a Relative error between calculated emission energy and experimental results at 77 K.

The characterization for these complexes mirrors that found for similar ppy-type and atl-type charged heteroleptic iridium complexes.^{3,12b} The effect of substitution on the relative energies of the HOMO and LUMO and its impact on the HOMO–LUMO gap are summarized in Figure 7. The replacement of the ppy-type ligand for the atl-type ligand results in destabilization of both the HOMO and the LUMO energies with a resulting net increase in the overall energy gap, supporting that observed by CV (Figure 8). The large influence on the LUMO energy is surprising given the paucity of electron density localized on the

atl in the LUMO. The replacement of the bpy for the dtBuppy ligand results in an expected destabilization of both the HOMO and the LUMO with a resulting small increase in the overall energy gap. As had been previously demonstrated,^{34,41} the incorporation of fluorine atoms results in a net increase in the HOMO–LUMO gap resulting from stabilization of both frontier MOs, with the energy of the HOMO being more significantly influenced. The calculated increase in the energy gap, corroborated both by CV and spectroscopic measurements (see Tables 3 and 4), is due to the synergistic effect of the addition of fluorine atoms, the incorporation of electron releasing *t*-butyl groups, and the presence of the triazole moiety. Thus, **4b** has the largest calculated energy gap of 3.46 eV.

Table 5 lists the dominant low energy singlet–singlet vertical excitations, their oscillator strengths, and a synopsis of their corresponding assignments for each of the 8 complexes under study. A comparison of the calculated and experimental absorption spectra for **2a**, **2b** and **4a**, **4b** is presented in Figure 9. The calculated absorption spectra agree well with experiment, notwithstanding that predicted spectra obtained by TD-DFT methods are frequently red-shifted.⁴² In all 8 complexes, the HOMO–LUMO transition is not permissible ($f \leq 0.0002$) nor was it observed in the experimental absorption spectra. The low intensity absorption transitions observed at $>300\text{ nm}$ can now be assigned unequivocally as mixed singlet MLCT/LLCT transitions. The tailings at about $>420\text{ nm}$, where singlet–singlet transitions are dark, can then be inferred to be spin-forbidden triplet excitations. From an analysis of the electron density distribution of the ³HSOMOs, these transitions can in part be assigned as ³MLCT/³LLCT (see Jablonski plots in Supporting Information, Figures S17–S24). The strongly absorbing higher energy transitions are LC in

nature, wherein the localization of electron density can either be C[^]N-based or N[^]N based.

The PL spectra at RT shown in Figure 3 are clearly broad and featureless, thus indicating that the character of emission remains essentially unchanged and is charge-transfer in nature. This assignment is supported by evaluation of the nature of the ³HSOMO for each of the complexes (see Supporting Information). Though we also estimated emission energies by calculating the vertical energy differences between the lowest triplet state and the S₀ singlet ground state, a more precise method is to take the difference between the total energy of the complex in the T₁ state, whose geometry is optimized at that state, and the total energy of the complex in the ground S₀ state, optimized at that state using UB3LYP methods without symmetry restrictions.³ These results are summarized in Table 6 and are compared to the measured E_{0,0} band obtained at 77 K in 1:1 MeOH/EtOH. Predictions are generally accurate though are slightly bathochromically shifted from experimental values.

CONCLUSIONS

Herein, we synthesized two sets of cationic heteroleptic iridium(III) complexes bearing aryltriazole ligands obtained via “Click” chemistry. Their photophysical and electrochemical properties were characterized, and their electronic behavior was compared to benchmark complexes bearing arylpyridine cyclometallating ligands. The experimental data is corroborated by a computational study. The combined investigation reveals that the use of 4-aryl-1-benzyl-1H-1,2,3-triazoles as cyclometallating ligands results in a net blueshift in the PL spectrum and an increase in the ΔE_{red-ox} in the CV. The result of this hypsochromicity is due to a destabilization of both the HOMO and the LUMO, wherein in the latter it is more pronounced. As well, a noted increase in PL quantum yield was observed due in part to the protective nature of the benzyl groups. Color tuning was found to be facile, and complexes in this study exhibit colors ranging from yellow to sky-blue. Given the ease and synthetic generality of the ligand synthesis, aryl triazoles may well become common replacements for ppy-type ligands.

ASSOCIATED CONTENT

S Supporting Information. Summary of crystallographic parameters and ORTEP diagrams for **2a**, **3b**, and **4a**. Absorption and emission spectra at 298 and 77 K for each of the 8 complexes. Cyclic voltammograms for each of the 8 complexes. Full computational output, including figures of calculated absorption spectra, tables of 100 lowest energy transitions calculated by TD-DFT and tables of calculated emission energies and isodensity surface plots for selected orbitals of each of the 8 complexes. ¹H and ¹³C NMR for each of the 8 complexes. Crystallographic files (CIF) for **2a**, **3b**, and **4a**. This material is available free of charge via the Internet at <http://pubs.acs.org>.

AUTHOR INFORMATION

Corresponding Author

*E-mail: Eli.Zysman-Colman@USherbrooke.ca.

ACKNOWLEDGMENT

Computational time on the Mammouth supercomputer at the Université de Sherbrooke was underwritten by the RQCHP (réseau québécois de calculs de haute performance). E.Z.-C.

acknowledges CFI (Canadian Foundation for Innovation), NSERC (the National Sciences and Engineering Research Council of Canada), FQRNT (Le Fonds québécois de la recherche sur la nature et les technologies), and the Université de Sherbrooke for financial support. S.L. acknowledges the Université de Sherbrooke for an institutional scholarship.

REFERENCES

- (1) (a) Garces, F. O.; King, K. A.; Watts, R. J. *Inorg. Chem.* **1988**, 27, 3464. (b) Ichimura, K.; Kobayashi, T.; King, K. A.; Watts, R. J. *J. Phys. Chem.* **1987**, 91, 6104. (c) King, K. A.; Watts, R. J. *J. Am. Chem. Soc.* **1987**, 109, 1589. (d) Ohsawa, Y.; Sprouse, S.; King, K. A.; DeArmond, M. K.; Hanck, K. W.; Watts, R. J. *J. Phys. Chem.* **1987**, 91, 1047. (e) Wilde, A. P.; King, K. A.; Watts, R. J. *J. Phys. Chem.* **1991**, 95, 629. (f) Wilde, A. P.; Watts, R. J. *J. Phys. Chem.* **1991**, 95, 622.
- (2) (a) For recent reviews see: Flamigni, L.; Barbieri, A.; Sabatini, C.; Ventura, B.; Barigelletti, F. *Top. Curr. Chem.* **2007**, 281, 143. (b) Ulbricht, C.; Beyer, B.; Friebe, C.; Winter, A.; Schubert, U. S. *Adv. Mater.* **2009**, 21, 4418. (c) Liu, Z.; Bian, Z.; Huang, C. *Top. Organomet. Chem.* **2010**, 28, 113.
- (3) Ladouceur, S.; Fortin, D.; Zysman-Colman, E. *Inorg. Chem.* **2010**, 49, 5625, and references cited therein.
- (4) (a) Yeh, S. J.; Wu, M. F.; Chen, C. T.; Song, Y. H.; Chi, Y.; Ho, M. H.; Hsu, S. F.; Chen, C. H. *Adv. Mater.* **2005**, 17, 285. (b) Chen, H.-Y.; Yang, C.-H.; Chi, Y.; Cheng, Y.-M.; Yeh, Y.-S.; Chou, P.-T.; Hsieh, H.-Y.; Liu, C.-S.; Peng, S.-M.; Lee, G.-H. *Can. J. Chem.* **2006**, 84, 309. (c) Yang, C.-H.; Li, S.-W.; Chi, Y.; Cheng, Y.-M.; Yeh, Y.-S.; Chou, P.-T.; Lee, G.-H.; Wang, C.-H.; Shu, C.-F. *Inorg. Chem.* **2005**, 44, 7770. (d) Ho, M.-L.; Hwang, F.-M.; Chen, P.-N.; Hu, Y.-H.; Cheng, Y.-M.; Chen, K.-S.; Lee, G.-H.; Chi, Y.; Chou, P.-T. *Org. Biomol. Chem.* **2006**, 4, 98. (e) He, L.; Duan, L.; Qiao, J.; Wang, R.; Wei, P.; Wang, L.; Qiu, Y. *Adv. Funct. Mater.* **2008**, 18, 2123.
- (5) (a) He, L.; Duan, L.; Qiao, J.; Dong, G.; Wang, L.; Qiu, Y. *Chem. Mater.* **2010**, 22, 3535. (b) Tamayo, A. B.; Garon, S.; Sajoto, T.; Djurovich, P. I.; Tsyba, I. M.; Bau, R.; Thompson, M. E. *Inorg. Chem.* **2005**, 44, 8723.
- (6) He, L.; Qiao, J.; Duan, L.; Dong, G.; Zhang, D.; Wang, L.; Qiu, Y. *Adv. Funct. Mater.* **2009**, 19, 2950.
- (7) Baranoff, E.; Fantacci, S.; De Angelis, F.; Zhang, X.; Scopelliti, R.; Grätzel, M.; Nazeeruddin, M. K. *Inorg. Chem.* **2010**, 50, 451.
- (8) (a) van Diemen, J. H.; Haasnoot, J. G.; Hager, R.; Müller, E.; Reedijk, J. *Inorg. Chim. Acta* **1991**, 181, 245. (b) Orselli, E.; Kottas, G. S.; Konradsson, A. E.; Coppo, P.; Fröhlich, R.; De Cola, L.; van Dijken, A.; Büchel, M.; Börner, H. *Inorg. Chem.* **2007**, 46, 11082. (c) Avilov, I.; Minoofar, P.; Cornil, J. r. m.; De Cola, L. *J. Am. Chem. Soc.* **2007**, 129, 8247. (d) Zhang, X.; Xu, Y.; Sun, Y.; Shi, H.; Zhu, X.; Cao, Y. *Thin Solid Films* **2007**, 515, 7347.
- (9) Lai, W.-Y.; Levell, J. W.; Jackson, A. C.; Lo, S.-C.; Bernhardt, P. V.; Samuel, I. D. W.; Burn, P. L. *Macromolecules* **2010**, 43, 6986.
- (10) Stagni, S.; Colella, S.; Palazzi, A.; Valenti, G.; Zacchini, S.; Paolucci, F.; Marcaccio, M.; Albuquerque, R. Q.; De Cola, L. *Inorg. Chem.* **2008**, 47, 10509.
- (11) (a) Richardson, C.; Fitchett, C. M.; Keene, F. R.; Steel, P. J. *Dalton Trans.* **2008**, 2534. (b) Obata, M.; Kitamura, A.; Mori, A.; Kameyama, C.; Czaplowska, J. A.; Tanaka, R.; Kinoshita, I.; Kusumoto, T.; Hashimoto, H.; Harada, M.; Mikata, Y.; Funabiki, T.; Yano, S. *Dalton Trans.* **2008**, 3292. (c) Li, Y.; Huffman, J. C.; Flood, A. H. *Commun.* **2007**, 2692. (d) Schulze, B.; Friebe, C.; Hager, M. D.; Winter, A.; Hoogenboom, R.; Gölrs, H.; Schubert, U. S. *Dalton Trans.* **2009**, 787. (e) Happ, B.; Escudero, D.; Hager, M. D.; Friebe, C.; Winter, A.; Gölrs, H.; Altuntas, E.; González, L.; Schubert, U. S. *J. Org. Chem.* **2010**, 75, 4025. (f) Fletcher, J. T.; Bumgarner, B. J.; Engels, N. D.; Skoglund, D. A. *Organometallics* **2008**, 27, 5430.
- (12) (a) Felici, M.; Contreras-Carballada, P.; Smits, J. M. M.; Nolte, R. J. M.; Williams, R. M.; De Cola, L.; Feiters, M. C. *Molecules* **2010**, 15, 2039. (b) Beyer, B.; Ulbricht, C.; Escudero, D.; Friebe, C.; Winter, A.; González, L.; Schubert, U. S. *Organometallics* **2009**, 28, 5478.

- (c) Fernández-Hernández, J. M.; Yang, C.-H.; Beltrán, J. I.; Lemaure, V.; Polo, F.; Fröhlich, R.; Cornil, J.; De Cola, L. *J. Am. Chem. Soc.* **2011**, *133*, 10543. (d) de Barros e Silva Botelho, M.; Fernandez-Hernandez, J. M.; de Queiroz, T. B.; Eckert, H.; De Cola, L.; de Camargo, A. S. *J. Mater. Chem.* **2011**, *21*, 8829.
- (13) (a) Felici, M.; Contreras-Carballada, P.; Vida, Y.; Smits, J. M. M.; Nolte, R. J. M.; Cola, L. D.; Williams, R. M.; Feiters, M. C. *Chem.—Eur. J.* **2009**, *15*, 13124. (b) Mydlak, M.; Bizzarri, C.; Hartmann, D.; Sarfert, W.; Schmid, G.; De Cola, L. *Adv. Funct. Mater.* **2010**, *20*, 1812. (c) Orsell, E.; Albuquerque, R. Q.; Fransen, P. M.; Frohlich, R.; Janssen, H. M.; Cola, L. D. *J. Mater. Chem.* **2008**, *18*, 4579.
- (14) Ladouceur, S.; Soliman, A. M.; Zysman-Colman, E. *Synthesis* **2011**, accepted for publication.
- (15) Kröhnke, F. *Synthesis* **1976**, 1.
- (16) Nonoyama, M. *Bull. Chem. Soc. Jpn.* **1974**, *47*, 767.
- (17) Costa, R. D.; Ortl, E.; Bolink, H. J.; Graber, S.; Schaffner, S.; Neuburger, M.; Housecroft, C. E.; Constable, E. C. *Adv. Funct. Mater.* **2009**, *19*, 3456.
- (18) Slinker, J. D.; Gorodetsky, A. A.; Lowry, M. S.; Wang, J.; Parker, S. T.; Rohl, R.; Bernhard, S.; Malliaras, G. G. *J. Am. Chem. Soc.* **2004**, *126*, 2763.
- (19) Bolink, H. J.; Coronado, E.; Costa, R. n. D.; Lardiés, N.; Orti, E. *Inorg. Chem.* **2008**, *47*, 9149.
- (20) Flack, H. D.; Blanc, E.; Schwarzenbach, D. J. *Appl. Crystallogr.* **1992**, *25*, 455.
- (21) Gabe, E. J.; Le Page, Y.; Charland, J.-P.; Lee, F. L.; White, P. S. *J. Appl. Crystallogr.* **1989**, *22*, 384.
- (22) Sheldrick, G. M. *SHELXS-97*, Release 97-2 ed.; University of Göttingen: Göttingen, Germany, 1997.
- (23) Frisch, M. J.; Trucks, G. W.; Schlegel, H. B.; Scuseria, G. E.; Robb, M. A.; Cheeseman, J. R.; Zakrzewski, V. G.; Montgomery, J. A.; Stratmann, R. E.; Burant, J. C.; Dapprich, S.; J.M., M.; Daniels, A. D.; Kudin, K. N.; Strain, M. C.; Farkas, O.; Tomasi, J.; Barone, V.; Cossi, M.; Cammi, R.; Mennucci, B.; Pomelli, C.; Adamo, C.; Clifford, S.; Ochterski, J.; Peterson, G. A.; Ayala, P. Y.; Cui, Q.; Morokuma, K.; Malik, A.; Rabuck, A. D.; Raghavachari, K.; Foresman, J. B.; Cioslowski, J.; Ortiz, J. V.; Baboul, A. G.; Stefanov, B. B.; Liu, G.; Liashenko, A.; Piskorz, P.; Komaromi, I.; Gomperts, R.; Martin, R. L.; Challacombe, M.; Gill, P. M. W.; Johnson, B. G.; Chen, W.; Wong, M. W.; Andres, J. L.; Head-Gordon, M.; Replogle, E. S.; Pople, J. A. *Gaussian 98* (Revision A.6); Gaussian Inc.: Pittsburgh, PA, 1998.
- (24) (a) Hohenberg, P.; Kohn, W. *Phys. Rev.* **1964**, *136*, B864. (b) Kohn, W.; Sham, L. J. *Phys. Rev.* **1965**, *140*, A1133. (c) In *The Challenge of d and f Electrons*; Salahub, D. R.; Zerner, M. C., Eds.; ACS: Washington, DC, 1989; (d) Parr, R. G.; Yang, W. *Density-functional theory of atoms and molecules*; Oxford Univ. Press: Oxford, U.K., 1989.
- (25) (a) Stratmann, R. E.; Scuseria, G. E.; Frisch, M. J. *J. Chem. Phys.* **1998**, *109*, 8218. (b) Bauernschmitt, R.; Ahlrichs, R. *Chem. Phys. Lett.* **1996**, *256*, 454. (c) Casida, M. E.; Jamorski, C.; Casida, K. C.; Salahub, D. R. *J. Chem. Phys.* **1998**, *108*, 4439.
- (26) (a) Becke, A. D. *J. Chem. Phys.* **1993**, *98*, 5648. (b) Lee, C.; Yang, W.; Parr, R. G. *Phys. Rev. B* **1988**, *37*, 785. (c) Miehlich, B.; Savin, A.; Stoll, H.; Preuss, H. *Chem. Phys. Lett.* **1989**, *157*, 200.
- (27) (a) Binkley, J. S.; Pople, J. A.; Hehre, W. J. *J. Am. Chem. Soc.* **1980**, *102*, 939. (b) Gordon, M. S.; Binkley, J. S.; Pople, J. A.; Pietro, W. J.; Hehre, W. J. *J. Am. Chem. Soc.* **1982**, *104*, 2797. (c) Pietro, W. J.; Franch, M. M.; Hehre, W. J.; Defrees, D. J.; Pople, J. A.; Binkley, J. S. *J. Am. Chem. Soc.* **1982**, *104*, 5039. (d) Dobbs, K. D.; Hehre, W. J. *J. Comput. Chem.* **1986**, *7*, 359. (e) Dobbs, K. D.; Hehre, W. J. *J. Comput. Chem.* **1987**, *8*, 861. (f) Dobbs, K. D.; Hehre, W. J. *J. Comput. Chem.* **1987**, *8*, 880.
- (28) (a) Stevens, W. J.; Basch, W. J.; Krauss, M. J. *J. Chem. Phys.* **1984**, *81*, 6026. (b) Stevens, W. J.; Krauss, M.; Basch, H.; Jasien, P. G. *Can. J. Chem.* **1992**, *70*, 612. (c) Cundari, T. R.; Stevens, W. J. *J. Chem. Phys.* **1993**, *98*, 5555.
- (29) Lowry, M. S.; Hudson, W. R.; Pascal, R. A., Jr.; Bernhard, S. *J. Am. Chem. Soc.* **2004**, *126*, 14129.
- (30) O'Boyle, N. M. *GaussSum 2.0*; Dublin City University: Dublin, Ireland, 2006; Available at <http://gausssum.sf.net>.
- (31) Crosby, G. A.; Demas, J. N. *J. Phys. Chem.* **1971**, *75*, 991.
- (32) Ishida, H.; Tobita, S.; Hasegawa, Y.; Katoh, R.; Nozaki, K. *Coord. Chem. Rev.* **2010**, *254*, 2449.
- (33) Connelly, N. G.; Geiger, W. E. *Chem. Rev.* **1996**, *96*, 877.
- (34) Lowry, M. S.; Goldsmith, J. I.; Slinker, J. D.; Rohl, R.; Pascal, R. A.; Malliaras, G. G.; Bernhard, S. *Chem. Mater.* **2005**, *17*, 5712.
- (35) The reported complex is $[\text{ppy-F}_2]_2\text{Ir}(\text{dtBubpy})^+$, where ppy-F₂ is 2,4-difluorophenylpyridinato. See ref 19.
- (36) Colombo, M. G.; Hauser, A.; Güdel, H. U. *Inorg. Chem.* **1993**, *32*, 3088.
- (37) Li, J.; Djurovich, P. I.; Alleyne, B. D.; Yousufuddin, M.; Ho, N. N.; Thomas, J. C.; Peters, J. C.; Bau, R.; Thompson, M. E. *Inorg. Chem.* **2005**, *44*, 1713.
- (38) Di Censo, D.; Fantacci, S.; De Angelis, F.; Klein, C.; Evans, N.; Kalyanasundaram, K.; Bolink, H. J.; Gratzel, M.; Nazeeruddin, M. K. *Inorg. Chem.* **2008**, *47*, 980.
- (39) Bolink, H. J.; Cappelli, L.; Coronado, E.; Grätzel, M.; Orti, E.; Costa, R. D.; Viruela, P. M.; Nazeeruddin, M. K. *J. Am. Chem. Soc.* **2006**, *128*, 14786.
- (40) Su, H.-C.; Wua, C.-C.; Fang, F.-C.; Wong, K.-T. *Appl. Phys. Lett.* **2006**, *89*, 261118.
- (41) Costa, R. D.; Viruela, P. M.; Bolink, H. J.; Ortí, E. *J. Mol. Struct.: THEOCHEM* **2009**, *912*, 21.
- (42) Dreuw, A.; Head-Gordon, M. *Chem. Rev.* **2005**, *105*, 4009.